

Supporting Information

A facile, one-step electroless deposition of NiFeOOH nanosheets onto photoanodes for highly durable and efficient solar water oxidation

*Mahesh P. Suryawanshi^{a,†}, Seung Wook Shin^{b,†}, Uma V. Ghorpade^a, Jihun Kim^c, Hye Won
Jeong^d, Soon Hyung Kang^e, Jin Hyeok Kim^{a,*}*

^aDepartment of Materials Science and Engineering and Optoelectronics Convergence Research Center, Chonnam National University, 300, Yongbong-Dong, Buk-Gu, Gwangju 61186, South Korea.

^bDepartment of Physics and Astronomy and Wright Center for Photovoltaic Innovation and Commercialization, University of Toledo, Toledo, Ohio, 43606, United States.

^cSchool of Electrical Engineering and Computer Science, Gwangju Institute of Science and Technology, 123 Cheomdangwagi-ro, Buk-gu, Gwangju 61005, South Korea.

^dSchool of Energy Engineering, Kyungpook National University, Daegu, Republic of Korea.

^eDepartment of Chemistry Education and Optoelectronics Convergence Research Center, Chonnam National University, 300, Yongbong-Dong, Buk-Gu, Gwangju 61186, South Korea.

† These authors contributed equally to this work.

* Corresponding author (Jin Hyeok Kim), Email: jinhyeok@chonnam.ac.kr; TEL: 82-62-530-1709, Fax: 82-62-530-1699

Experimental Section

Chemicals and Materials. Iron (II) chloride tetrahydrate ($\text{FeCl}_2 \cdot 4\text{H}_2\text{O}$, 99%), Nickel (II) nitrate hexahydrate ($\text{Ni}(\text{NO}_3)_2 \cdot 6\text{H}_2\text{O}$, 98%), hexamethyltetramine (HMTA, 99%), sodium hydroxide (NaOH, 97%), Titanium (IV) butoxide, hydrochloric acid (HCl, 35 ~ 37%) were obtained from Sigma-Aldrich and used as received. Fluorine-doped SnO_2 (FTO) glass substrates with resistivity of 6~8 $\Omega \cdot \text{cm}^{-2}$ were obtained from Pilkington TEC glassTM.

Preparation of TiO_2 NR Arrays. Rutile TiO_2 NR arrays on FTO glass were synthesized using a well-developed hydrothermal method.^{1, 2} Briefly, equal 11.3 mL volumes of DI water and HCl were mixed for 5 min., followed by the incorporation of 0.189 mL of Titanium (IV) butoxide. The solution was subsequently transferred to a Teflon-lined stainless-steel autoclave. Afterwards, several pieces of the cleaned FTO substrate were placed at an angle against the wall of the Teflon-liner. The hydrothermal treatment was performed at 150 °C for 9 h in a vacuum oven. After the reaction was finished, the autoclave was naturally cooled down to room temperature, and the sample was cleaned using DI water several times, finally dried using nitrogen gas. To enhance the crystallinity of the as-synthesized TiO_2 NR arrays, a post-thermal treatment was carried out at 450 °C for 30 min. in an ambient air. The photographs of the TiO_2 and $\text{TiO}_2/\text{NiFeOOH}$ samples are shown in Fig. S1.

Deposition of NiFeOOH Nanosheets onto FTO Substrates and TiO_2 Nanorod (NR) Arrays

Electrodes. Prior to the deposition, FTO substrates was prepared and cleaned via ultra-sonication by sequentially immersing the substrate in deionized (DI) water, ethanol, and acetone for 20 min. in each step to remove some of the organic contamination and dust. A facile, room temperature electroless deposition was further used for the deposition of NiFeOOH nanosheets onto FTO or TiO_2 NR arrays onto FTO substrates. First of all, two separate solutions of $\text{FeCl}_2 \cdot 4\text{H}_2\text{O}$ (2×10^{-3}

M) and $\text{Ni}(\text{NO}_3)_2 \cdot 6\text{H}_2\text{O}$ (2×10^{-3} M) in deionized water (DI) were prepared. Furthermore, 5×10^{-3} M of HMTA was added to both solutions under constant stirring at 400 rpm/min. to serve as complexing agent to retards the rate of hydroxide precipitation at room temperature. Next the stock solution was prepared in polypropylene bottle (60 ml) at room temperature by mixing appropriate amounts of $\text{FeCl}_2 \cdot 4\text{H}_2\text{O}$ and $\text{Ni}(\text{NO}_3)_2 \cdot 6\text{H}_2\text{O}$ with $[\text{Ni}^{2+}/(\text{Fe}^{3+} + \text{Ni}^{2+})]$ ratio ranging from 5 to 125. Note, that a large $[\text{Ni}^{2+}/(\text{Fe}^{3+} + \text{Ni}^{2+})]$ ratio was used to incorporate the Ni^{2+} into FeOOH since the solubility product constant of $\text{Ni}(\text{OH})_2$ is much larger than that of FeOOH . Then FTO or TiO_2 NR grown on FTO substrates were kept inclined by 45°C in the stock solution in polypropylene bottle. Subsequently, an equal volume of NaOH (20×10^{-3} M) was added slowly to the stock solution in polypropylene bottle without stirring. The polypropylene bottles were then sealed and maintained at room temperature to proceed the reaction for desired reaction times such as 5, 10, 20, 40 min. The similar experimental procedure was employed to integrate NiFeOOH nanosheets onto TiO_2 NR arrays on FTO substrate. The resulting $\text{TiO}_2/\text{NiFeOOH}$ core/shell nanostructured photoanodes were removed from the solutions, rinsed with the deionized water and further dried under N_2 flow. The electroless deposition of NiFeOOH proceeds through a ligand-controlled oxidation reaction. We suppose that the complex formed between metal species ($\text{M}^{\text{II/III}}$) and HMTA ligand in the precursor solution avoids the deposition of $\text{M}^{\text{II}}(\text{OH})_2/\text{M}^{\text{III}}(\text{OH})_3$ even after addition of NaOH solution. The metal species preferentially coordinates the ligands rather than hydroxide ions from NaOH solution; however, dissolved metal species M^{II} were also present owing to the equilibrium between metal species and complex between metal species and ligand. These dissolved metal species M^{II} would undergo oxidation to M^{III} by dissolved oxygen under alkaline condition without the ligand. On the other hand, it is quite difficult to change the oxidation state of M^{II} , when M^{II} species are coordinated to the ligands. Thus, “ligand-controlled oxidation” of metal species would

form the oxyhydroxide rather than the hydroxides or layered double hydroxides due to their low solubility.

Material Characterization. The structural properties of the nanostructures were examined by X-ray diffraction (XRD), using a XRD, PANalytical, X'Pert-PRO Netherlands operated at 45 kV, 40 mA, and room temperature. The chemical states of nanostructures were examined using a high-resolution X-ray photoelectron spectroscope (HR-XPS, VG Multi lab 2000, Thermo VG Scientific, UK) at room temperature. The binding energies were calibrated using the carbon 1s line at 285.0 eV. Field Emission Scanning Electron Microscopy (FE-SEM) using (FE-SEM, S4800, HITACHI Inc.) operating at 10 kV and 20 mA and High-resolution Transmission electron microscopy (HR-TEM) using JEOL-3010 with an acceleration voltage of 300 kV and located at the Korean Basic Science Institute (KBSI, Gwangju, South Korea) was used to observe the morphology of nanostructures. The elements distribution was investigated by scanning TEM (STEM) and high-angle annular dark-field imaging in the STEM (HAADF-STEM) located at KBSI, Gwangju, and South Korea. TEM samples were prepared by drop casting technique using nanostructured powders collected by scratching the NiFeOOH nanosheets from TiO₂ NR onto FTO substrates dispersed in ethanol onto carbon meshed nickel TEM grids (200 meshes, Structure Probe, Inc.). The UV-Visible spectra of nanostructures were obtained with Cary 100 (Agilent, Australia) spectrometer at room temperature.

Photoelectrochemical (PEC) Measurements. For PEC-oxygen evolution reaction (OER) measurements, all measurements were carried out using Autolab potentiostat (CHI Instruments, USA) in a three-electrode compression cell under simulated solar light illumination (AM 1.5G, 100 mW/cm²). The photoanodes serve as working electrodes, which were front illuminated with an active area of 0.2 cm² defined by the mask in PEC cell. The reference and counter electrodes

were an Ag/AgCl (3.5 M KCl) electrode and Pt foil, respectively. 0.01 M Na₂SO₄ was used as electrolyte which was bubbled with N₂ for 30 min. prior to measurement. For all photoanodes, the current-voltage (*J-V*) curves under chopped light on/off illumination and without chopped light illumination were performed at a scan rate of 20 mV/s during the potential sweep. The photoconversion efficiency (η) was calculated according to the equation (Eq.(1)):

$$\eta = J \times (1.23 - E_{RHE}) / P_{light} \quad \text{Eq. (1)}$$

where, *J* is the photocurrent density at the measured potential and *P_{light}* is the irradiation intensity of 100 mW/cm². The calibration was performed using an NREL-certified silicon photodiode. The Ag/AgCl reference electrode was calibrated to the reversible hydrogen electrode (RHE) and the potentials in the 0.01 M Na₂SO₄ solution is expressed by the standard Nernst equation (Eq.(2))

$$E_{RHE} = E_{Ag/AgCl} + 0.05916 \times pH + E^0 \quad \text{Eq. (2)}$$

where, *E_{RHE}* is the potential vs. RHE, *E_{Ag/AgCl}* is the measured potential vs. Ag/AgCl and *E⁰* = 0.2 V at 25 °C. The incident photon to current efficiency (IPCE) was measured in the wavelength range of 300 ~ 550 nm at a potential of 0.5 V vs. the sat. Ag/AgCl electrode using a specially designed IPCE system for PEC water splitting. Herein, a 150 W Xenon lamp was used as the light source for generating the monochromatic beam. The IPCE was calculated using the equation (Eq.(3)):

$$IPCE = (1240 \times J_{mono}) / (P_{mono} \times \lambda) \quad \text{Eq. (3)}$$

where, *J_{mono}* is the measured photocurrent density at a specific wavelength; *P_{mono}* is the measured irradiance at a specific wavelength, and λ is the wavelength of incident light.

Electrochemical impedance spectroscopy (EIS) was performed in same electrochemical configuration and electrolyte under the condition of 1 sun illumination on an Autolab PGSTAT

equipped with an FRA2 frequency response analyzer with Nova 1.7 controlled data acquisition under open-circuit voltage. The EIS measurements were carried out in potentiostat mode at open circuit potential in the frequency range from 0.1 Hz to 100 kHz with an amplitude of ± 10 mV. Each EIS spectrum were modeled using the suggested equivalent circuit as shown in Figure S5 by using the Zview program with relative errors below 5%. A chronoamperometry test was conducted on the $\text{TiO}_2/\text{NiFeOOH}$ core/shell nanostructured photoanode at 1.23 V (vs RHE) under simulated AM 1.5G illumination. The quantitative analysis of evolved O_2 was carried out using gas chromatography (Agilent, 7890B) equipped with a thermal conductivity detector and a molecular sieve 5A column. An air-tight three electrode PEC reactor with an Ag/AgCl reference electrode, Pt as a counter electrode and the photoanodes as working electrodes was used for gas chromatography measurements. Before the measurements, the reactor was pre-purged by N_2 gas (>99.9%) for 1 h to remove O_2 from electrolyte and headspace (25 ml). The $\text{TiO}_2/\text{NiFeOOH}$ photoanode was biased at 0.6 V (vs. Ag/AgCl) in a stirred aqueous solution of 0.01 M Na_2SO_4 (pH = ~ 7) under AM 1.5G simulated sunlight. The charge separation and charge transfer efficiencies were calculated as a function of the applied potential by adding 0.5 M Na_2SO_3 in the electrolyte as a hole scavenger. We assume that the oxidation kinetics of Na_2SO_3 is very fast and its charge transfer efficiency is 100%. Therefore, ratio of adsorbed photocurrent density of semiconductor and photocurrent density measured in Na_2SO_3 gives rise to the charge-separation efficiency, whereas ratio of photocurrent densities measured in H_2O and Na_2SO_3 gives rise to charge-transfer efficiency. The absorbed photocurrent density of about 1.87 mA/cm² for TiO_2 is considered for the calculation of charge separation and transfer efficiency of TiO_2 NR photoanode. On the other hand, the charge separation and transfer efficiency of $\text{TiO}_2/\text{NiFeOOH}$ NR photoanode were calculated by integrating the optimal spectrum over the entire solar spectrum. The CV curves were measured in

non-Faradaic region at various scan rates (10, 20, 40, 60 and 80 mV. S⁻¹) for TiO₂ and TiO₂/NiFeOOH. The charging current density differences (J) between the anodic (J_a) and cathodic charging current densities in the middle of the potential window was plotted against the scan rate, and the linear slope is twice of Cdl. The electrochemical active surface area (ECSA) is then calculated from Cdl according to the equation of ECSA = Cdl/Cs, where Cs is the specific capacitance of the sample. The electrochemical performance of NiFeOOH deposited on glassy carbon electrode (GCE) was measured in 1.0 M KOH (pH= 14) using a standard three electrode configuration using Autolab potentiostat (CHI Instruments, USA) at room temperature. The active area of working electrode was 2 cm².

Work Function Measurements: Ultraviolet photoelectron spectroscopy (UPS) was employed to determine the work functions of FTO, TiO₂ and NiFeOOH. The UPS spectra were recorded on a Kratos AXIS-NOVA Ultra DLD using nonmonochromatized He-I α radiation (UPS, $h\nu = 21.22$ eV). The work functions were determined from the secondary electron cut-off (SEC) using the equation $WF = 21.22 \text{ eV} - \text{SEC}$. The difference between the Fermi levels and valence band maximum (VBM) were determined from the low binding energy onset.

Table S1. Comparison of the photocurrent densities and stabilities between TiO₂/NiFeOOH core/shell nanostructured photoanode and previously reported Earth-abundant oxyhydroxides/layered double hydroxides-based OECs shell onto various core structured photoanodes.

Catalyst	Photoanode	Catalyst deposition method	J _{sc} with OEC (mA/cm ²)	J _{sc} without OEC (mA/cm ²)	Stability test	Ref.
Co-Ni LDH	ZnO NRs	Electro-deposition	1.52 at 0.5 V _{Ag/AgCl}	0.3 at 0.5 V _{Ag/AgCl}	-	S3
Ni-Fe LDH	Ta ₃ N ₅ NRs	Hydrothermal	1.7 at 1.23 V _{RHE}	1.0 at 1.23 V _{RHE} 2.0 V _{RHE}	~ 10% decay after 2 h	S4
Co-Al LDH	Fe ₂ O ₃ NRs	Hydrothermal	2.0 at 1.23 V _{RHE}	0.3 at 1.23 V _{RHE}	No decay after 2 h	S5
FeOOH	BiVO ₄ film	Photo-deposition	1.8 at 1.23 V _{RHE}	0.1 at 1.23 V _{RHE}	~ 2% decay after 2 h	S6
FeOOH	Nanoporous Mo:BiVO ₄ film	Photo-deposition	2.77 at 1.23 V _{RHE}	2.41 at 1.23 V _{RHE}	-	S7
FeOOH	Mo:BiVO ₄ film	Photoelectro-deposition	2.9 at 1.23 V _{RHE}	0.5 at 1.23 V _{RHE}	~ 20% decay after 6 h	S8
NiOOH	Coral-like Fe ₂ O ₃	Photoelectro-deposition	0.625 at 1.23 V _{RHE}	0.425 at 1.23 V _{RHE}	~ 20% decay after 12 h	S9
FeOOH	Fe ₂ O ₃ NRs	Precipitation	1.21 at 1.23 V _{RHE}	0.612 at 1.23 V _{RHE}	<3% decay after 2.5 h	S10
NiOOH	(Sn, Zr) Fe ₂ O ₃ NRs	Photoelectro-deposition	1.65 at 1.23 V _{RHE}	0.86 at 1.23 V _{RHE}	~ 6% decay after 10 h	S11
CoOOH	Mg-Ta ₃ N ₅ NRs	Electrodeposition	6.5 at 1.23 V _{RHE}	2.0 at 1.23 V _{RHE}	~ 30% decay after 1.13h	S12
FeOOH/NiOOH	Nanohelix WO ₃ /(W, Mo) BiVO ₄	Photoelectro-deposition	5.3 at 1.23 V _{RHE}	3.8 at 1.23 V _{RHE}	<1% decay after 12 h	S13

FeOOH/ NiOOH	Nanocone- Mo:BiVO ₄	Electrodeposition	5.82 at 1.23 V _{RHE}	3.45 at 1.23 V _{RHE}	No decay after 5 h	S14
FeOOH/ NiOOH	Nanoporous BiVO ₄ film	Electrodeposition	2.73 at 1.23 V _{RHE}	1.4 at 1.23 V _{RHE}	No decay after 48 h	S15
Ni:FeOOH	WO ₃ /BiVO ₄ NWs	Hydrothermal	4.5 at 1.23 V _{RHE}	4.0 at 1.23 V _{RHE}	No decay after 3 h	S16
Zn-Fe LDH	TiO ₂ NTs	Photoelectro- deposition	1.51 at 1.23 V _{RHE}	0.79 at 1.23 V _{RHE}	<5% decay after 10 h	S17
Ni-Fe LDH	TiO ₂ NRs	Electrodeposition	1.18 at 0.6 V _{SCE}	0.92 at 0.6 V _{SCE}	<3% decay after 3 h	S18
NiFeOOH	TiO₂ NRs	One-step electroless deposition	3.85 at 1.23 V_{RHE}	0.73 at 1.23 V_{RHE}	<5% decay after 24 h	This work

LDH: Layered double hydroxide; NRs: Nanorods; NTs: Nanotubes; NWs: Nanowires



Fig. S1. The photographs of TiO₂ and TiO₂/NiFeOOH samples.

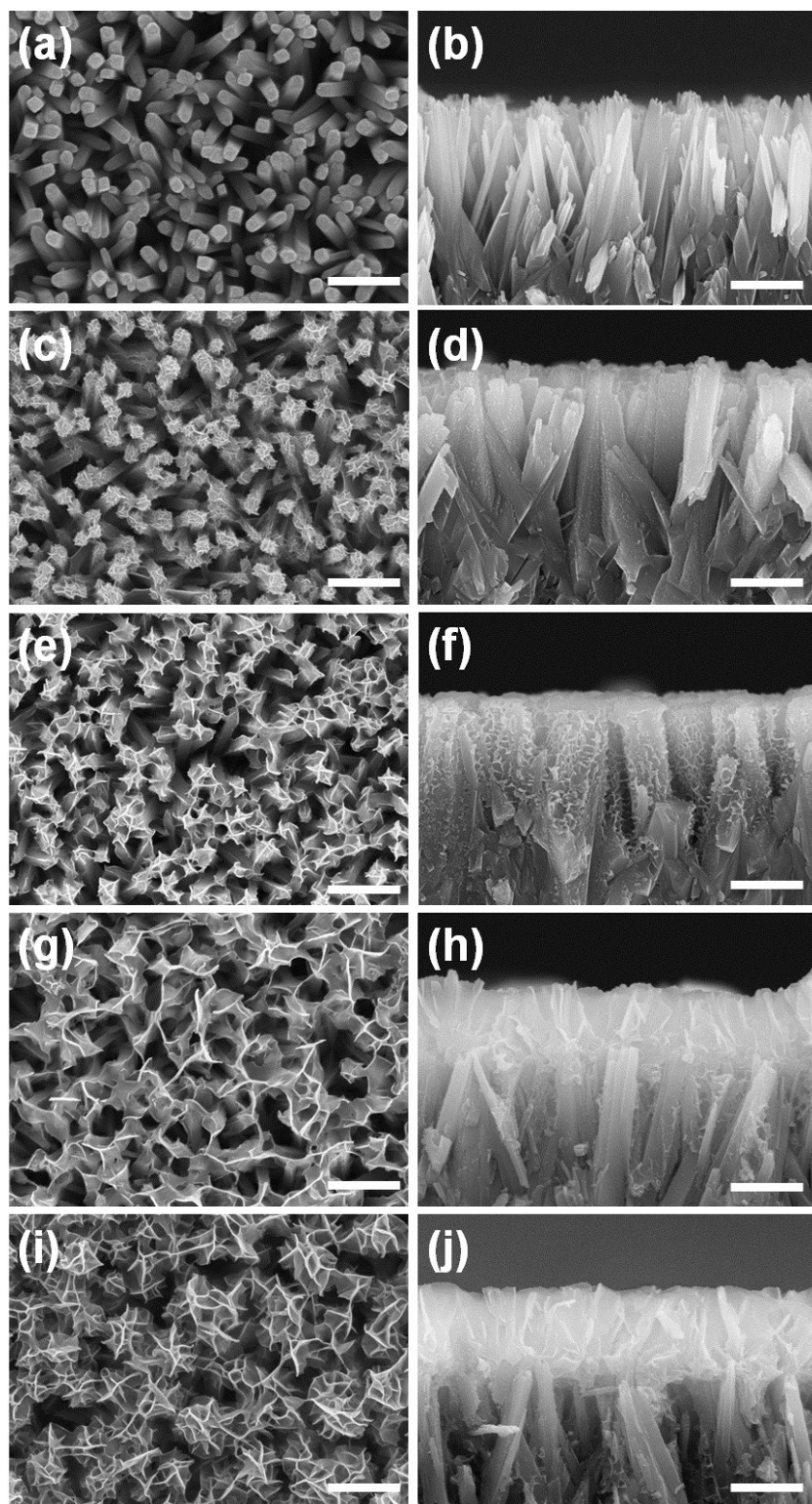


Fig. S2. Surface and cross-sectional FE-SEM images of (a and b) TiO₂ NR and NiFeOOH nanosheets grown onto the TiO₂ NRs at the different deposition times of (c and d) 5 min, (e and f) 10 min, (g and h) 20 min, and (i and j) 40 min. All Scale bars are 500 nm.

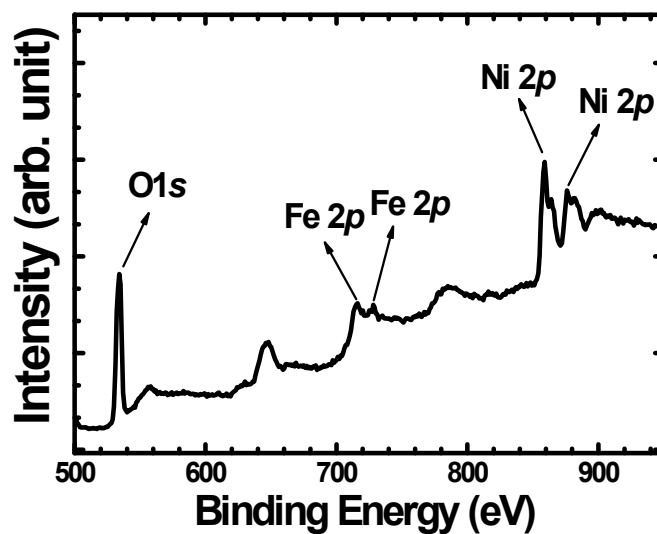


Fig. S3. XPS survey spectrum of NiFeOOH nanosheet on FTO substrate deposited for the reaction time of 10 min.

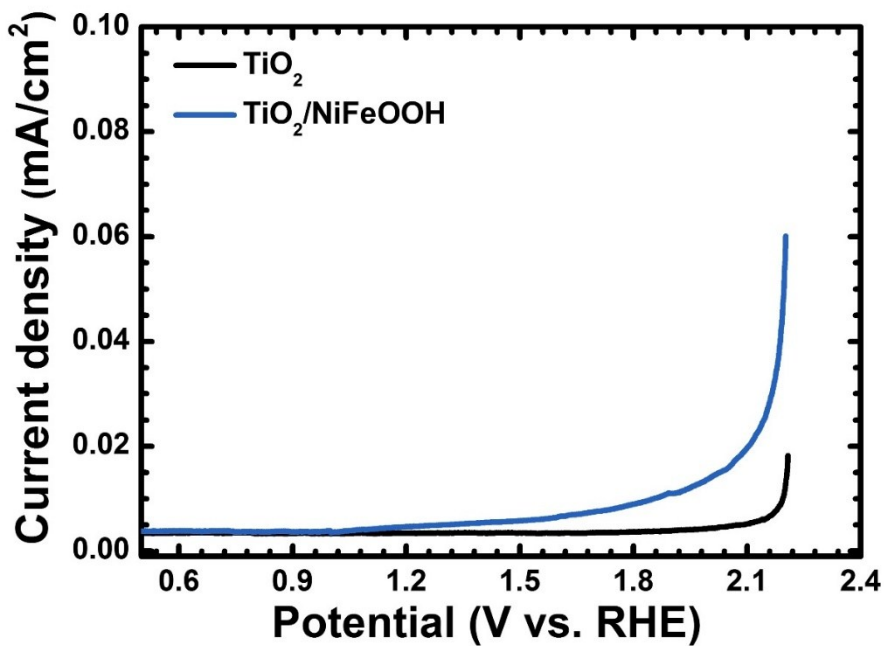


Fig. S4. J - V curves of TiO_2 and $\text{TiO}_2/\text{NiFeOOH}$ core/shell nanostructured photoanodes measured in 0.01 M Na_2SO_4 aqueous electrolyte (pH \sim 7) at dark condition.

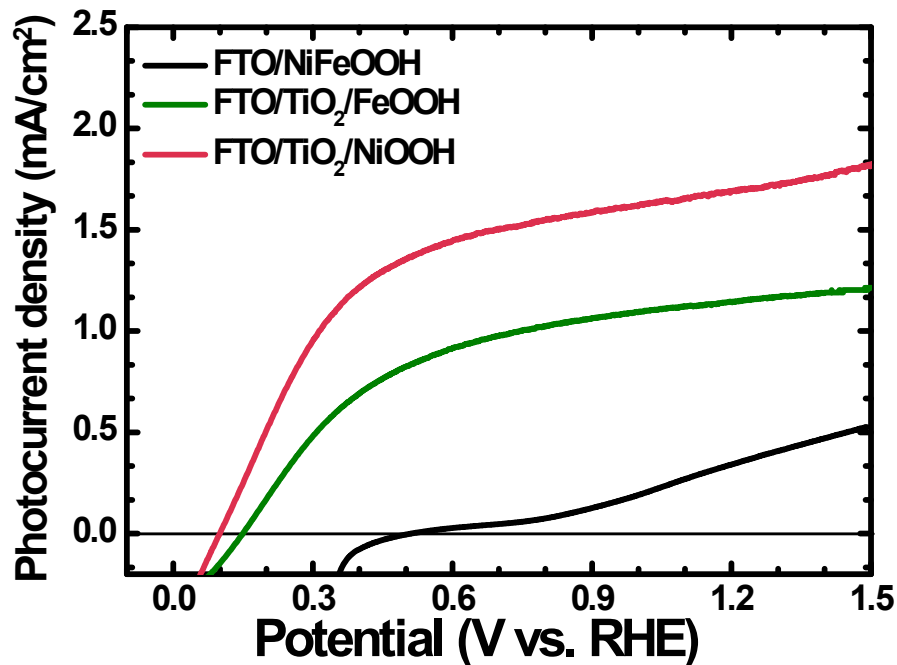


Fig. S5. PEC performances of (a) FTO/NiFeOOH, (b) FTO/TiO₂/FeOOH, and (c) FTO/TiO₂/NiOOH photoanodes. All the performances were measured in 0.01 M Na₂SO₄ electrolyte under AM 1.5G illumination for solar water oxidation

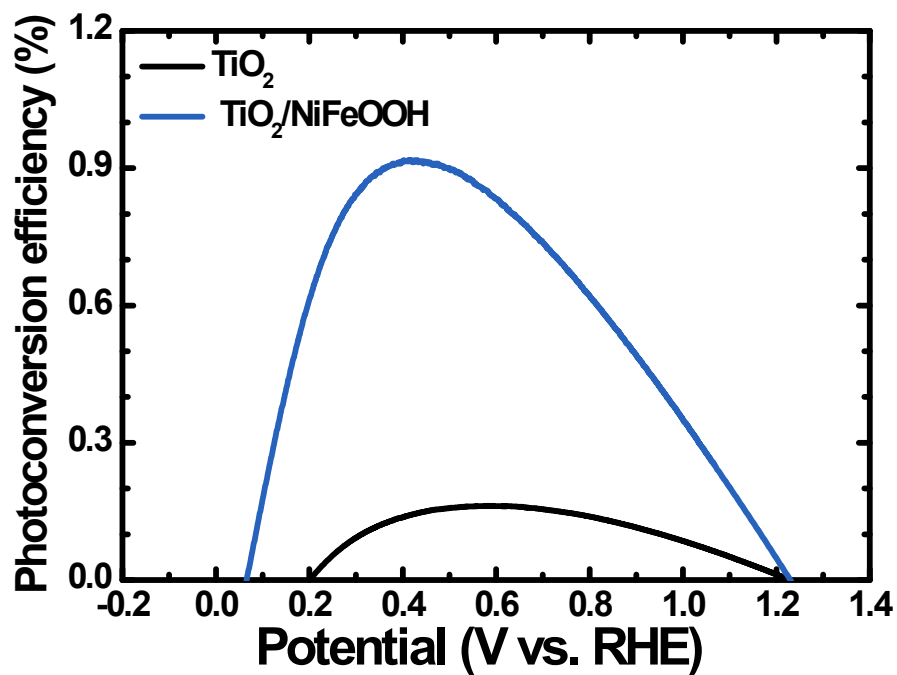


Fig. S6. Photoconversion efficiencies as of TiO₂ and TiO₂/NiFeOOH photoanodes a function of the

applied potential.

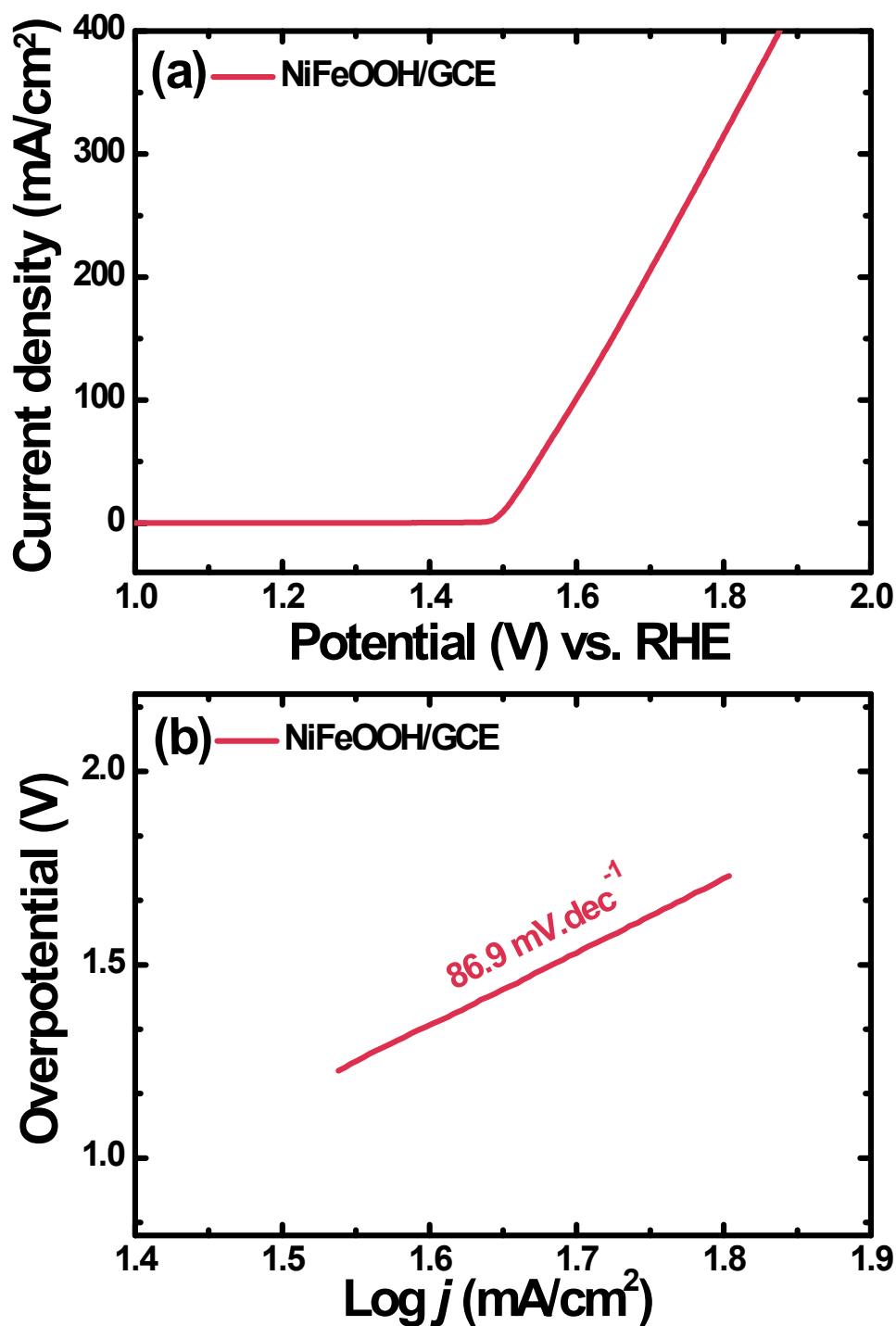


Fig. S7. Electrocatalytic performance of NiFeOOH catalysts. (a) OER polarization curve of NiFeOOH deposited onto GCE in 1.0 M KOH (pH= ~ 14) at 10 mV s⁻¹, and (b) Tafel slope of NiFeOOH/GCE catalysts.

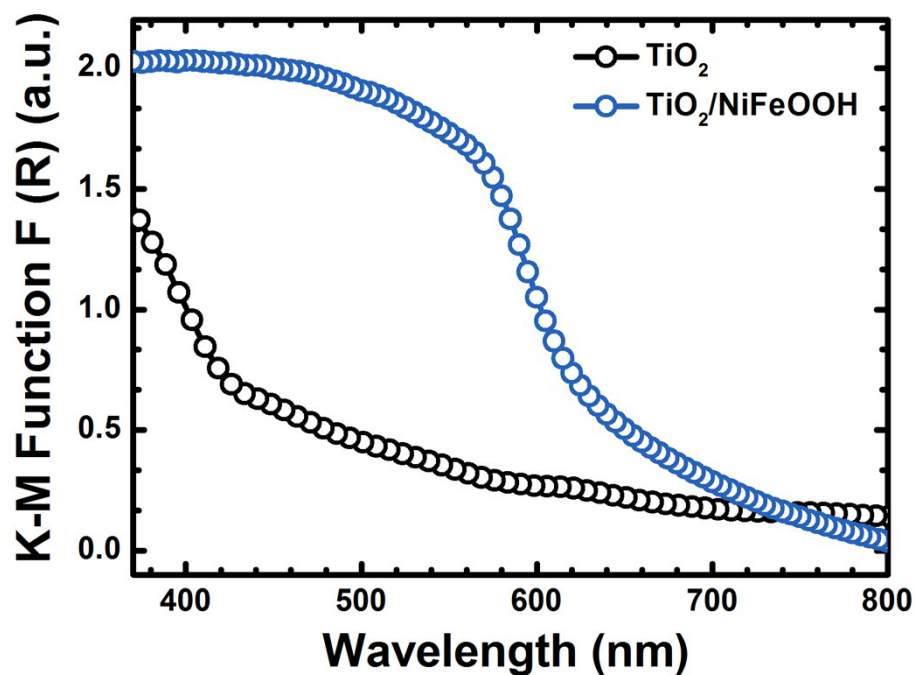


Fig. S8. UV-Vis diffused reflectance spectra (DRS) of TiO_2 NRs and $\text{TiO}_2/\text{NiFeOOH}$ core/shell nanostructured photoanodes.

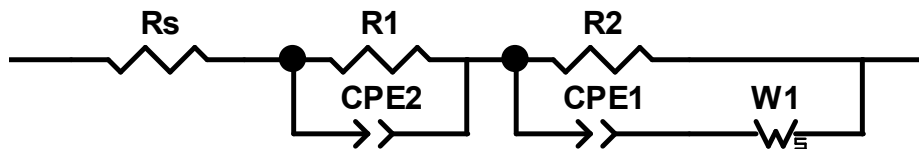


Fig. S9. The equivalent circuit model used to simulate the Nyquist plots from ESI measurements.

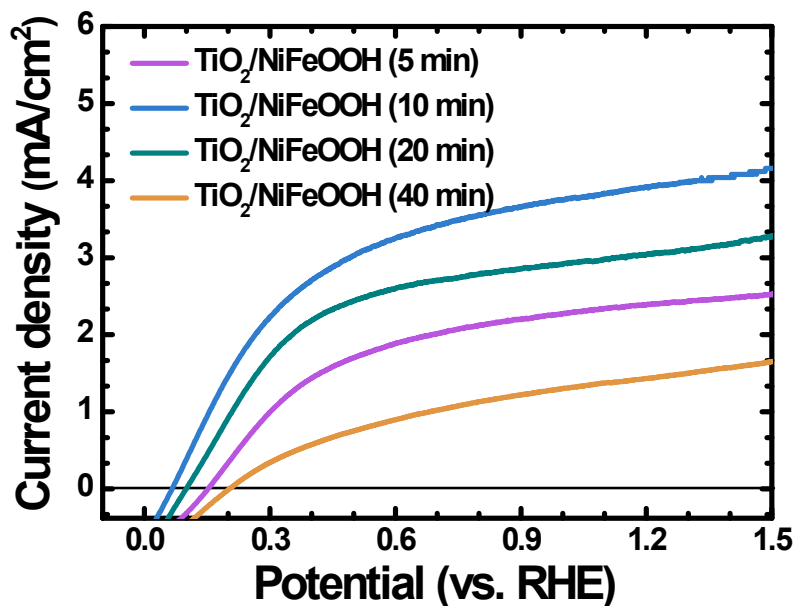


Fig. S10. J-V curves of TiO₂/NiFeOOH core/shell nanostructured photoanodes with different deposition times of NiFeOOH nanosheet measured under AM 1.5G illumination for solar water oxidation.

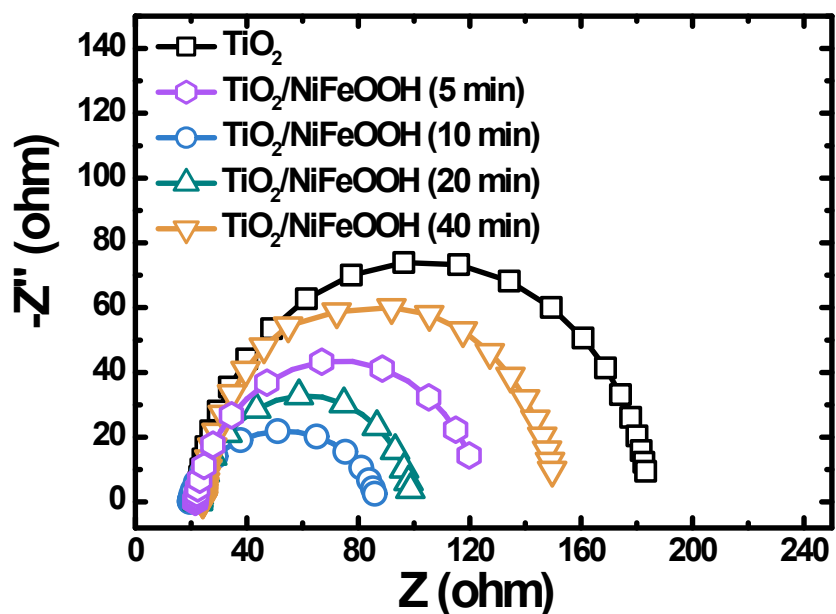


Fig. S11. The EIS spectra of pristine TiO₂ NR and TiO₂/NiFeOOH core/shell nanostructured photoanodes with different deposition times of NiFeOOH nanosheet measured under AM 1.5G illumination at open circuit potential over a frequency range of 0.1 Hz to 100 kHz with an amplitude of ± 10 mV.

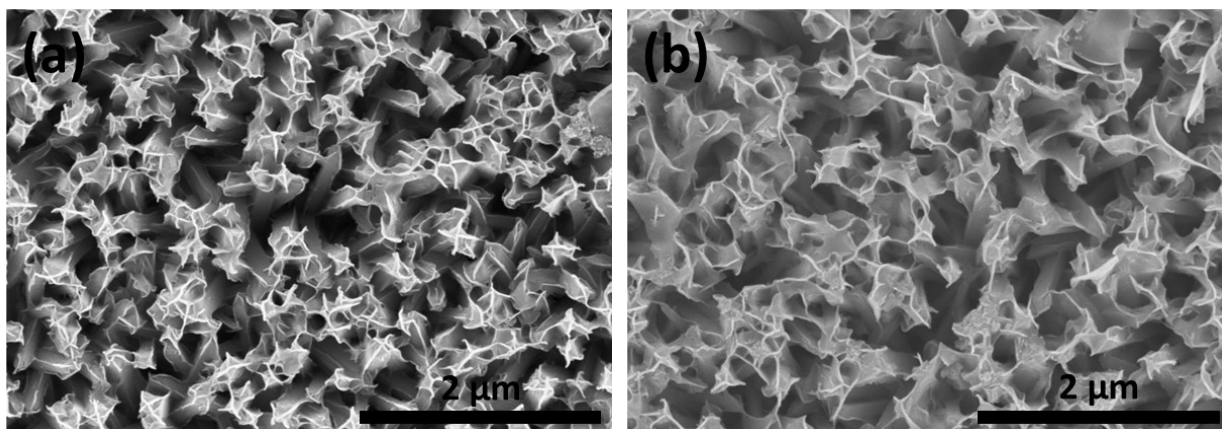


Fig. S12. FE-SEM image of $\text{TiO}_2/\text{NiFeOOH}$ core/shell nanostructured photoanode for 10 min. at room temperature (a) before and (b) after 24 h of stability test. No any significant changes were observed in the microstructure of $\text{TiO}_2/\text{NiFeOOH}$ core/shell nanostructured photoanode even after prolonged light illumination.

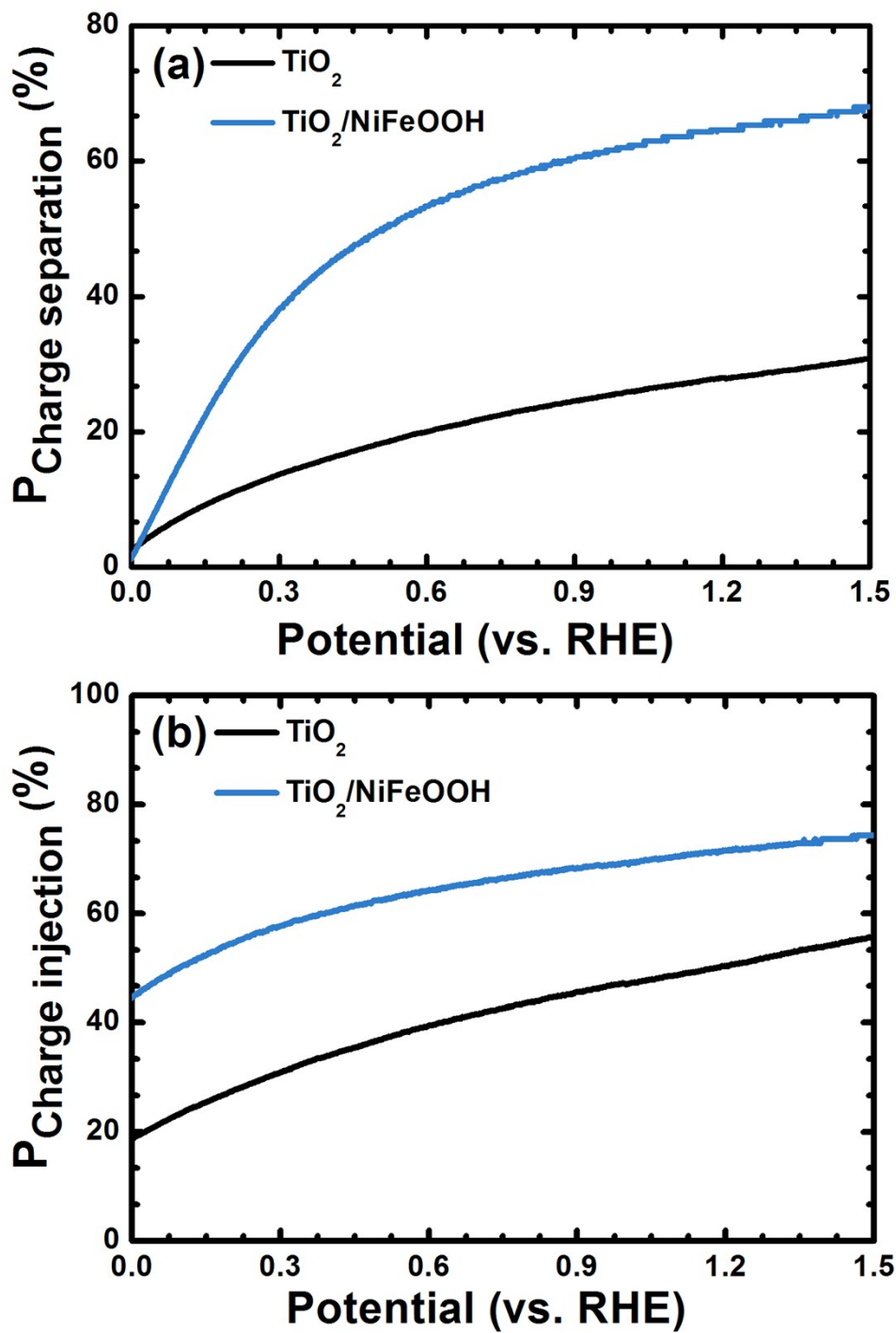


Fig. S13. (a) Charge-separation efficiency and (b) charge-injection (transfer) efficiency of the TiO_2 NR and $\text{TiO}_2/\text{NiFeOOH}$ core/shell nanostructured photoanodes

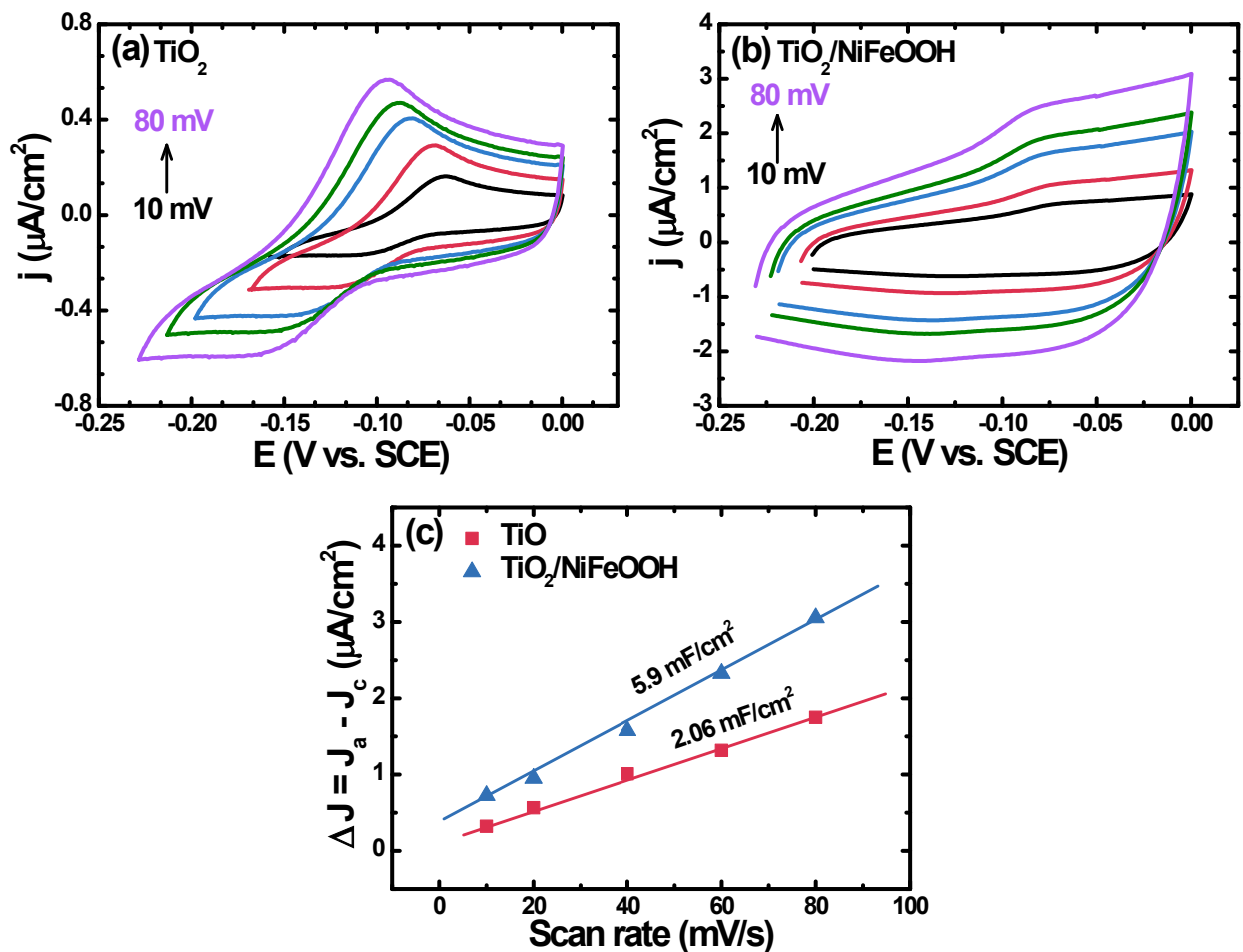


Fig. S14. CV curves of (a) TiO_2 NR, and (b) $\text{TiO}_2/\text{NiFeOOH}$ NR measured in the non-Faradaic region at various scan rates (10, 20, 40, 60, and 80 $\text{mV}\cdot\text{s}^{-1}$), and (c) Charging current densities differences ($\Delta J = J_a - J_c$) used for the double layer capacitance (C_{dl}) calculations and estimation of the relative ECSAs of TiO_2 and $\text{TiO}_2/\text{NiFeOOH}$ photoanodes.

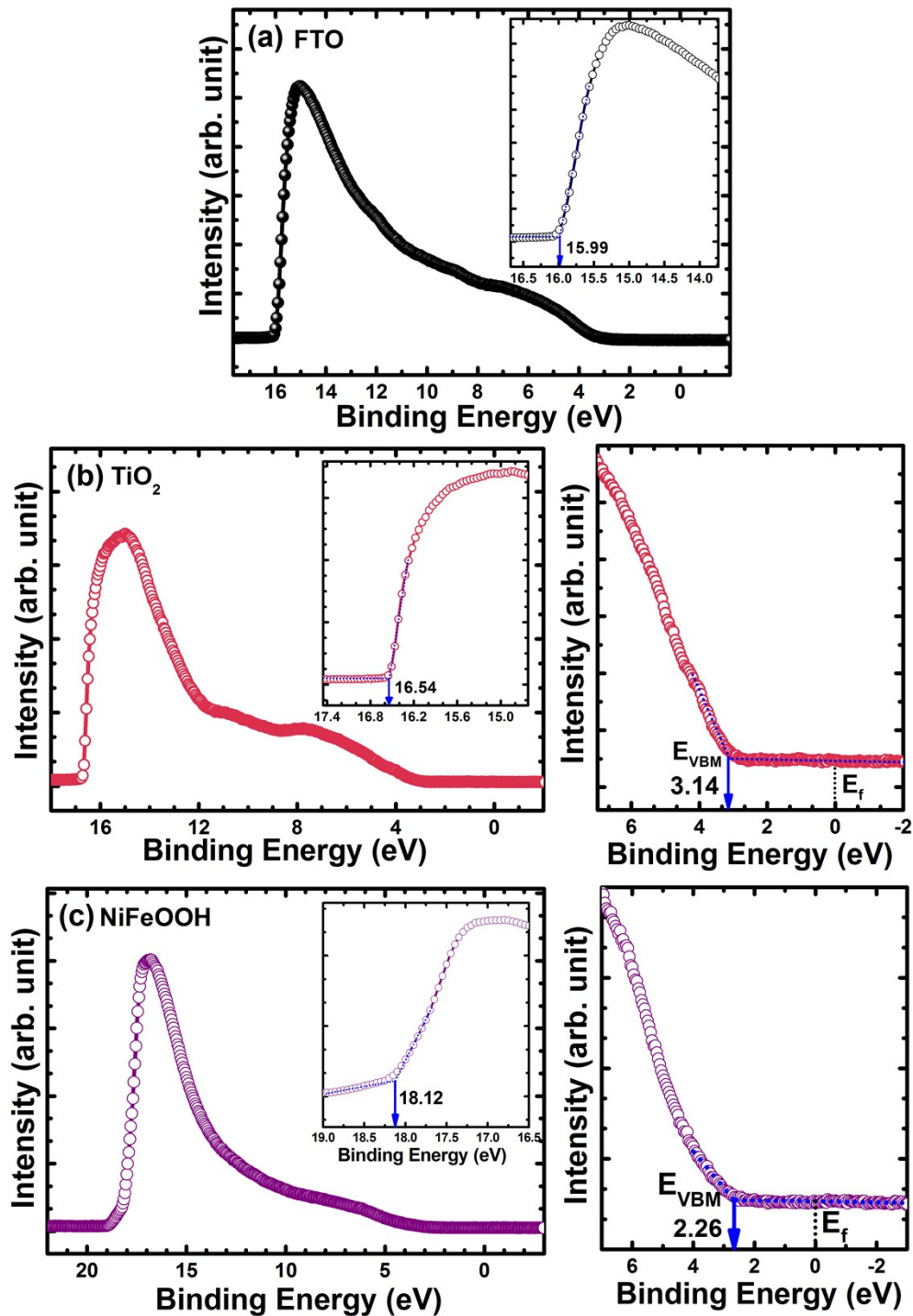


Fig. S15. UPS spectra of (a) FTO, (b) TiO₂ NRs and (c) NiFeOOH nanosheets. The inset of (a)-(c) shows the secondary electron cut-off energy, which is determined from the intersection of the linear portion of spectrum and the baseline. The right panel of (b) and (c) shows the magnified views of the low binding energy region for E_{VBM} determination.

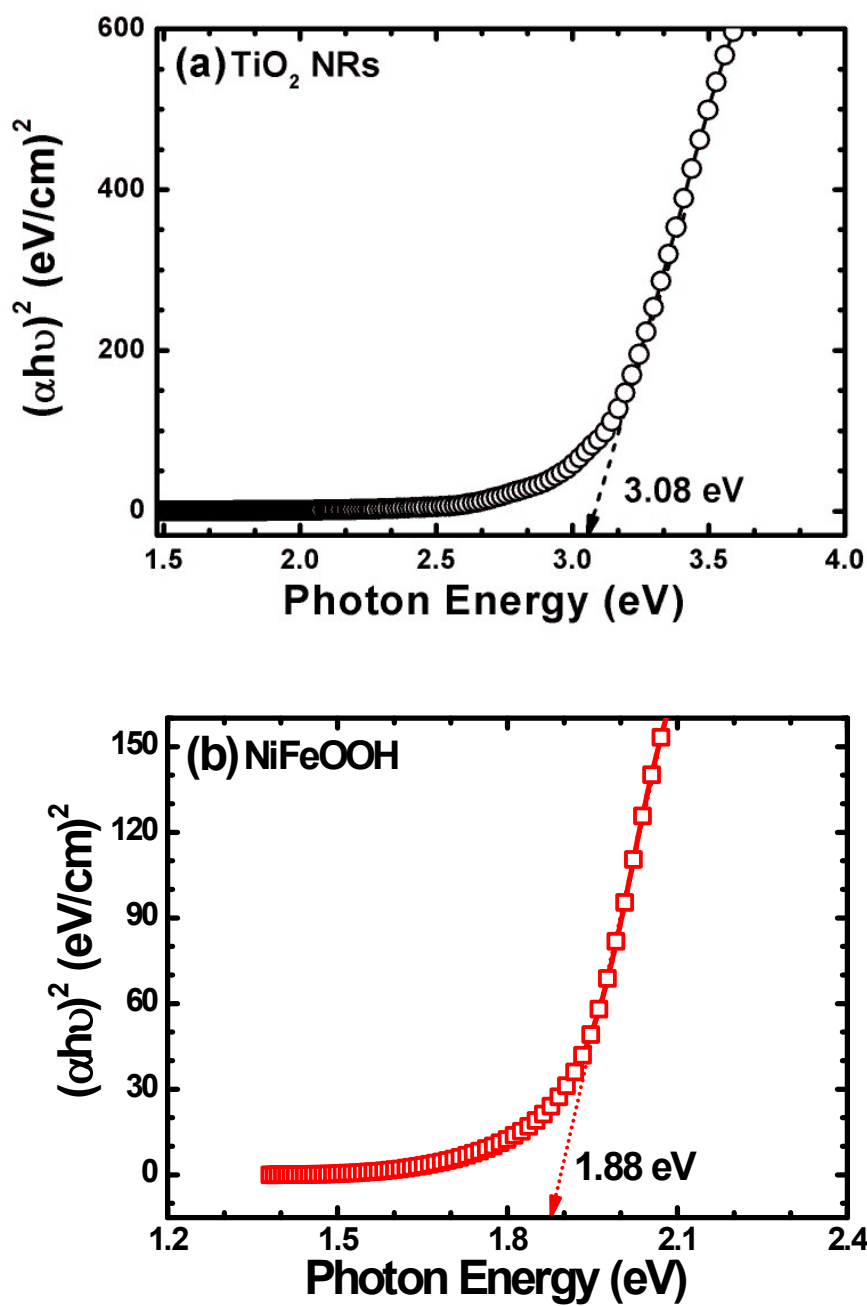


Fig. S16. The photon energy vs $(\alpha h\nu)^2$ plots of (a) TiO_2 NRs, and (b) NiFeOOH nanosheets grown on the FTO substrates.

Table S2. The values of work function, valence band maximum (VBM, E_{VBM}), conduction band minimum (CBM, E_{CBM}) and band gap energy (E_{g}) of FTO, TiO_2 NRs, and NiFeOOH nanosheets. E_{g} are obtained from Fig. S16.

Sample	Work function (eV)	E_{VBM} (eV)	E_{CBM} (eV)	E_{g} (eV)
FTO	-5.23	.	.	.
TiO_2	-4.68	-7.82	-4.74	3.08
NiFeOOH	-3.10	-5.36	-3.48	1.88

References for SI

- S1. M. Suryawanshi, S.W. Shin, U. Ghorpade, D. Song, C.W. Hong, S.S. Han, J. Heo, S.H. Kang and J.H. Kim, *J. Mater. Chem. A*, 2017, **5**, 4695.
- S2. S.W. Shin, M.P. Suryawanshi, H.K. Hong, G. Yun, D. Lim, J. Heo, H.K. Kang and J.H. Kim, *Electrochem. Acta*, 2016, **219**, 470
- S3. M. Shao, F. Ning, M. Wei, D. G. Evans and X. Duan, *Adv. Funct. Mater.*, 2014, **24**, 580.
- S4. L. Wang, F. Dionigi, N. T. Nguyen, R. Kirchgeorg, M. Gliech, S. Grigorescu, P. Strasser and P. Schmuki, *Chem. Mater.*, 2015, **27**, 2360.
- S5. R. Chong, B. Wang, C. Su, D. li, L. Mao, Z. Chang and L. Zhang, *J. Mater. Chem. A*, **2017**, **5**, 8583.
- S6. J. A. Seabold and K.-S. Choi, *J. Am. Chem. Soc.*, 2012, **134**, 2186.
- S7. J. A. Seabold, K. Zhu and N. R. Neale, *Phys. Chem. Chem. Phys.*, 2014, **16**, 1121.
- S8. L. Chen, F. M. Toma, J. K. Cooper, A. Lyon, Y. Lin, I. D. Sharp and J. W. Ager, *ChemSusChem*, 2015, **5**, 47080.
- S9. F. Malara, A. Minguzzi, M. Marelllo, S. Morandi, R. Psaro, V. D. Santo and A. Naldoni, *ACS Catal.*, 2015, **5**, 5292.
- S10. J. Y. Kim, D. H. Youn, K. Kang and J. S. Lee, *Angew. Chem. Int. Ed.*, 2016, **55**, 10854.
- S11. A. G. Tamirat, W.-N. Su, A. A. Dubale, H.-M. Chen and B.-J. Hwang, *J. Mater. Chem. A*, 2015, **3**, 5949.
- S12. L. Pei, Z. Xu, Z. Shi, H. Zhu, S. Yan and Z. Zou, *J. Mater. Chem. A*, **2017**, **5**, 20439.
- S13. X. Shi, I. Y. Choi, K. Zhang, J. Kwon, D. Y. Kim, J. K. Lee, S. H. Oh, J. K. Kim and J. H. Park, *Nat. Commun.*, 2014, **5**, 4775
- S14. Y. Qiu, W. Liu, W. Chen, G. Zhou, P.-C. Hsu, R. Zhang, Z. Liang, S. Fan, Y. Zhang and Y. Cui, *Sci. Adv.*, 2016, **2**, e1501764.
- S15. T. W. Kim and K.-S. Choi, *Science*, 2014, **343**, 990.
- S16. L. Cai, J. Zhao, H. Li, J. Park, I. S. Cho, H. S. Han and Z. Zheng, *ACS Energy Lett.*, 2016, **1**, 624.
- S17. R. Zhang, M. Shao, S. Xu, F. Ning, L. Zhou and M. Wei, *Nano Energy*, 2017, **33**, 21-28.
- S18. F. Ning, M. Shao, S. Xu, Y. Fu, R. Zhang, M. Wei, D. G. Evans and X. Duan, *Energy Environ. Sci.*, 2016, **9**, 2633-2643.